Skeletal Stem Cell-Schwann Cell Circuitry in Mandibular Repair

R. Ellen Jones[1,3], **Ankit Salhotra**[1,2,3], **Kiana S. Robertson**[1,2], **Ryan C. Ransom**[1,2], **Deshka S. Foster**[1], **Harsh N. Shah**[1,2], **Natalina Quarto**[1], **Derrick C. Wan**[1], **Michael T. Longaker**[1,2,4,*]

[1]Department of Surgery, Division of Plastic and Reconstructive Surgery, Stanford University School of Medicine, Stanford, CA 94305, USA

[2]Institute for Stem Cell Biology and Regenerative Medicine, Stanford University School of Medicine, Stanford, CA 94305, USA

[3]These authors contributed equally

[4]Lead Contact

SUMMARY

Regenerative paradigms exhibit nerve dependency, including regeneration of the mouse digit tip and salamander limb. Denervation impairs regeneration and produces morphological aberrancy in these contexts, but the direct effect of innervation on the stem and progenitor cells enacting these processes is unknown. We devised a model to examine nerve dependency of the mouse skeletal stem cell (mSSC), the progenitor responsible for skeletal development and repair. We show that after inferior alveolar denervation, mandibular bone repair is compromised because of functional defects in mSSCs. We present mSSC reliance on paracrine factors secreted by Schwann cells as the underlying mechanism, with partial rescue of the denervated phenotype by Schwann cell transplantation and by Schwann-derived growth factors. This work sheds light on the nerve dependency of mSSCs and has implications for clinical treatment of mandibular defects.

In Brief

Jones et al. demonstrate the nerve dependency of mandibular bone repair after degeneration of the inferior alveolar nerve. Schwann cell paracrine signaling is required for skeletal stem cell enactment of bone healing. Rescue of healing by Schwann cell transplantation highlights skeletal stem cell-Schwann cell circuitry during mandibular repair.

Graphical Abstract

Mandibular Bone with Intact Innervation

Osteotomy

Schwann Cell

Skeletal Stem Cell

Paracrine Circuitry

Mandibular Bone Repair

INTRODUCTION

Studies of amphibian limb amputation indicate the importance of innervation during regenerative processes. Whereas innervated limbs regenerate after proximal amputation, denervation leads to stump formation (Brockes, 1984). Lineage-restricted progenitors enact mouse digit tip regeneration in a nerve-dependent fashion (Rinkevich et al., 2011, 2014). The role of the autonomic nervous system in bone repair is well established: the neurotransmitters adenosine and epinephrine regulate osteoblasts (Costa et al., 2011; Gharibi et al., 2011; Ma et al., 2011), as do semaphorins (Li et al., 2017; Negishi-Koga et al., 2011). With regard to nerve-dependent bone regeneration, the morphologically impaired regeneration of denervated digits is linked to the absence of Schwann cells and their mitogens (Johnston et al., 2016). However, the effect of denervation on various stem cell populations responsible for mandibular repair has not been investigated.

Schwann cells are recognized for their active role in tissue repair (Carr et al., 2019; Clements et al., 2017; Johnston et al., 2016). Peripheral nerve injury triggers Wällerian degeneration, which entails proliferation and dedifferentiation of Schwann cells. If the axon is totally destroyed, Schwann cell presence eventually diminishes (Johnston et al., 2016; Weinberg and Spencer, 1978). This decrease in Schwann cells is linked to compromised regeneration, but the direct effects on putative stem and progenitor cells enacting regeneration remain unknown. Previous studies have determined that Schwann cell-derived paracrine factors, including platelet-derived growth factor-AA (PDGF-AA) and oncostatin

M (OSM), increase the regenerative capacity of the digit tip (Johnston et al., 2016). In this study, we tested the direct influence of denervation-induced Schwann cell paucity on the mouse skeletal stem cell (mSSC) during mandibular healing.

The mSSC hierarchy represents the family of progenitor cells responsible for producing bone and cartilage during axial and craniofacial skeletal bone regeneration, including during mandibular repair (Chan et al., 2015, 2018; Marecic et al., 2015; Ransom et al., 2018). The ability to prospectively isolate these cells allows us to investigate the cellular biology of mandibular repair, including nerve dependency. After devising a model of mandibular denervation by inferior alveolar nerve (IAN) disruption, we present evidence that mandibular healing is nerve dependent. We show that IAN disruption leads to Schwann cell paucity, resulting in impaired bone healing due to the functional deficiencies of mSSCs. The proposed mechanism for these findings is that mSSCs are dependent upon Schwann cell paracrine growth factors to promote mandibular repair.

RESULTS

Mouse Mandibular Denervation Model

We devised a model of mandibular denervation by proximal transection of the IAN (Figures 1A and 1B). The IAN was disrupted surgically, and this procedure was validated using $PLP::CreER^{T2};R26^{mTomato}$ (PLP Tomato) mice. PLP Tomato mice underwent IAN denervation or sham surgery and were imaged stereomicroscopically 2 weeks later. This confirmed IAN disruption, with significantly decreased mTomato expression in IAN denervated mice. (Figures 1A and 1C).

To understand histological changes associated with denervation, mandibular tissue sections from innervated and denervated mice were immunostained for proteolipid protein (PLP; green, Schwann cells) and protein gene product 9.5 (PGP9.5; red, axons). Confocal microscopy revealed significantly decreased PLP expression 2 weeks after IAN denervation, which was associated with degeneration of the nerve. Innervated specimens showed stable expression of PLP with intact tissue architecture. There were no differences in PGP9.5 expression between intact and disrupted IAN (Figures 1D and 1E). The depletion of Schwann cell signal over axonal signal led us to further examine the long-term appearance of denervation in PLP Tomato mice. Nerve degeneration and decreased mTomato expression persisted with a 6 month trace in a denervated mandible compared with the innervated control (Figures 1F and 1G). These studies confirmed that our surgical protocol successfully disrupted the IAN, with corresponding depletion of Schwann cells.

Mandibular Repair Is Nerve Dependent

We next tested the effect of IAN denervation on mandibular bone repair. Innervated and denervated mice underwent full-thickness osteotomy of the right hemimandible (Figure 2A). These were harvested at postoperative day (POD) 10, when pentachrome staining revealed ongoing tissue repair in innervated bone defects with mineralization of a cartilaginous intermediate (endochondral ossification; Ransom et al., 2018). This reparative response was absent in denervated mandibles (Figure 2B). Three-dimensional reconstruction of mandibles

scanned with micro-computed tomography (μCT) at PODs 10, 20, and 30 confirmed significant impairment in bone defect closure in denervated mandibles (Figures 2C and 2D). Alcian blue staining showed decreased cartilage formation in denervated mandibles compared with innervated mandibles at POD 10 (Figure 2E). Active healing seen in innervated POD 10 mandible defects was associated with increased EdU staining compared with uninjured bone, but this increase was significantly reduced in denervated mandible defects (Figures 2F and 2G). These findings suggest an underlying lack of cellular proliferation as a potential mechanism for poor healing in denervated mandibles.

Mandibular mSSC Kinetics Are Nerve Dependent

We investigated mSSC kinetics using fluorescence-activated cell sorting (FACS) to isolate mSSCs and characterize their function. Innervated and denervated mandibles were harvested at PODs 5,10,15, and 20 (Figure 3A), and mSSCs were isolated using FACS (Gulati et al., 2018). This uncovered a significantly diminished presence of mSSCs in denervated mandibles compared with innervated mandibles at PODs 10, 15, and 20 (Figure 3B). Across all PODs, the fractions of CD45+ and Ter119+ cells were similar between innervated and denervated specimens, suggesting that immune and angiogenic factors were similar between groups (Figure 3C). In addition, histologic examination and *in vivo* isolectin staining showed intact vasculature in both groups (Figure S1A); immunohistochemical CD34-positive staining was also comparable (Figure S1B). Profiling of downstream skeletal stem cell populations recapitulated the effect seen with mSSCs, with significant lack of expansion of bone-cartilage-stromal progenitor (BCSP) cells and osteoprogenitor (OP) cells in denervated mandible defects (Figures 3D and 3F). BCSP and OP cells were present in similar proportions of their parent cell population across the time points (Figures 3E and 3G), confirming an upstream deficiency in stem cells.

The function of denervated mSSCs was examined with *in vitro* assays. The number of colony-forming units (CFUs) was significantly lower from denervated versus innervated defects (Figure 3H). In addition, mSSCs harvested at POD 10 underwent osteogenic differentiation to quantify bone formation. Denervated mSSCs did not exhibit significant increase in osteogenic capacity, while innervated mSSCs did (compared with mSSC from uninjured mandibles; Figures 3I and 3J). The fate of mSSCs in our model appears to follow the presented hierarchy (Figure 3A, top). However, we cannot confirm the final fate of mSSCs, because of the lack of a mouse model to lineage trace mSSC.

Schwann Cell-mSSC Paracrine Interactions Drive Bone Repair

Our findings that Schwann cells deplete after denervation led us to focus upon this aspect of mSSC nerve dependency (Figures 1D and 1E). Previous reports led us to hypothesize that secreted signals from IAN Schwann cells underpin the nerve dependency of mSSC (Clements et al., 2017; Johnston et al., 2016). To test the paracrine influence of IAN Schwann cells on mandibular healing by mSSC, a co-culture experiment was performed (Figure 4A). mSSCs were isolated from denervated injured mandibles and seeded into cell culture wells. Concordantly, *PLP*-mTomato-positive Schwann cells were isolated from PLP Tomato mice (Figures S2A–S2C) and seeded onto the membrane of a hanging cell culture insert. The control group had only Schwann cell media placed into the insert. Fluorescent

microscopy confirmed the presence of mTomato-positive cells growing on the hanging insert (Figure 4B). CFUs between the two co-culture groups revealed significant rescue of mSSC CFUs by Schwann cells (Figure 4C).

We further investigated the role of Schwann cells in mandibular healing *in vivo* by transplanting PLP-mTomato-positive Schwann cells versus Matrigel vehicle alone into the mandible defect of denervated mice at the time of osteotomy. Engraftment of *PLP*-mTomato-positive Schwann cells was confirmed by tissue sectioning and confocal imaging (Figure 4D). µCT and pen-tachrome staining revealed significantly more bone formation in mandibles treated with *PLP*-mTomato-positive Schwann cells compared with defects treated with vehicle alone (Figures 4E–4H, top right). We confirmed that bone formation occurred in denervated defects after Schwann cell transplantation with immune staining for collagen 1 and RUNX2 (Figure S3F).

Transplanted Schwann cells were isolated from PLP Tomato mice on the basis of red fluorescence expression (Figure S2), which was maintained upon Schwann cell engraftment (Figure 4D). We thus hypothesized that these cells maintain intrinsic *PLP* positivity and Schwann cell identity after transplantation. To further examine the fate differentiation of *PLP*-mTomato-positive cells in our model, we created defects in innervated and denervated mandibles of PLP Tomato mice and harvested 4 weeks after osteotomy. Lineage tracing of PLP-positive cells *in vivo* revealed that there was no contribution of *PLP*-mTomato-positive cells to the healed bone of innervated or denervated mice (Figures S3A–S3C). Additionally, *PLP*-mTomato-positive Schwann cells did not engraft into bone or contribute directly to healed bone tissue after transplantation (Figure S3D). Transplanted *PLP*-mTomato-positive Schwann cells were located adjacent to the healing osteotomy in nearby soft tissue (Figure 4D). Additionally, transplanted *PLP*-mTomato-positive cells stained positively for S100, signifying that they maintain Schwann cell identity after engraftment (Figure S3E). Taken together, we conclude that *PLP*-mTomato-positive Schwann cells do not contribute directly to bone formation after injury or become mSSCs.

Next, we investigated specific Schwann-secreted ligands that may support mSSC function during mandibular healing. This study focuses on PDGF-AA, OSM, and parathyroid hormone (PTH). These growth factors and their receptors were selected for study on the basis of previously described implications in Schwann cell-dependent healing and mandibular fracture repair (Johnston et al., 2016; Ali et al., 2012; Jilka et al., 1999; Macica et al., 2006). Quantitative real-time PCR confirmed mSSC gene expression of receptors to these factors (Figure S4A). Additionally, *PLP*-mTomato-positive Schwann cells underwent quantitative real-time PCR, which confirmed gene expression of *PDGF-AA, PTH,* and *OSM* (Figure S4B). Taken together, these data imply that the nerve dependency of mandibular healing may be due partially to paracrine signaling of PDGF-AA, PTH, and OSM from Schwann cells to mSSCs (Figure S4C). Presence of receptors for these ligands in healing mandibular bone was further confirmed with immune staining from innervated and denervated mandibles (Figures S4D–S4F). Although our study cannot rule out that other mandibular tissue may supply these factors to support proper bone healing, it is clear that there is not sufficient compensatory paracrine signaling after denervation to promote healing.

Rescue of Mandibular Defects with Paracrine Factors

To further test the ability of Schwann cell paracrine factors, the *in vivo* effects of PDGF-AA, PTH, and OSM on denervated mandibular healing were examined. Each factor was separately suspended in Matrigel and injected into denervated mandibular defects at PODs 1 and 5. After harvesting at POD 10 and scanning with μCT, mandible bone formation was improved significantly, confirmed with histology of the osteotomy area (Figures 4H and 4I). These data suggest that mSSCs respond to Schwann cell-secreted growth factors to enact mandibular repair.

DISCUSSION

Previous work uncovered the crucial role of nerve-mediated tissue regeneration in the mouse digit tip (Carr et al., 2019; Johnston et al., 2016; Rinkevich et al., 2011). Our extensive study of mandibular distraction osteogenesis (DO) revealed that the mSSC enacts mandibular bone regeneration via mechanically induced activation of primitive neural crest cell transcriptional programs (Ransom et al., 2018). We questioned the role of innervation during mandibular repair, especially in light of the particular mandibular tissue complex with the IAN coursing through the bone itself. We present evidence that mSSCs require IAN Schwann cells to repair mandibular defects. Although previous studies create osteotomies to access and disrupt the IAN (Chiego et al., 1981; Zhao et al., 2014), our surgical protocol does not involve bone injury. We show that the denervated phenotype is associated with proliferative and functional impairment of mSSCs during bone repair. The dynamic bone repair process as carried out by mSSCs is halted by IAN denervation because of a lack of paracrine signaling between mSSCs and Schwann cells.

The predominance of neural crest-derived cells and neural crest-associated transcriptional programs during craniofacial development, regeneration, and repair is significant (Minoux et al., 2017). Peripheral nerves, which are derived from the neural crest, are essential to progenitor function during development and homeostasis of the mouse incisors (Kaukua et al., 2014; Zhao et al., 2014). Schwann cells contribute to diverse neuronal progenitor populations (Espinosa-Medina et al., 2014; Uesaka et al., 2015), and peripheral glia maintain salient roles in promoting both neuronal and non-neuronal tissue repair (Parfejevs et al., 2018; Richardson et al., 1980; Silva et al., 2018). This behavior is linked to Schwann cell transcriptional reprogramming and paracrine signaling by local Schwann cells (Clements et al., 2017; Johnston et al., 2016; Parfejevs et al., 2018). Although interaction between nervous and bony tissue during skeletal development and repair has been shown in several models (Aro, 1985; Dysart et al., 1989; Johnston et al., 2016; Recidoro et al., 2014; Rinkevich et al., 2011), our study directly links Schwann cells with mSSCs enacting mandibular bone repair. Clinically, mandibular fractures persist as a significantly challenging problem associated with high nerve injury and healing complication rates (Hsieh et al., 2019; Tay et al., 2015). Harnessing the underlying biology of nerve-dependent mandibular repair may hold promise for clinical innovation in mandible skeletal tissue repair, and we establish the importance mSSC and Schwann cell circuitry to facilitate mandibular healing. The mechanistic pathways by which mSSC and Schwann cells

cooperate to execute mandible healing remain of interest, including further study of additional Schwann-derived growth factors not covered in this work.

STAR★METHODS

LEAD CONTACT AND MATERIALS AVAILABILITY

This study did not generate new unique reagents. Further information and requests for resources and reagents should be directed to and will be fulfilled by the Lead Contact, Michael Longaker (longaker@stanford.edu).

EXPERIMENTAL MODEL AND SUBJECT DETAILS

The C57BL/6 (strain name C57BL/6, stock number 000664) WT mice used for wild-type studies were purchased from Jackson Laboratory. The *PLP::CreER^{T2}, Rosa26^{tdTomato}*, and NOD scid were purchased from Jackson Laboratory (strain name B6.Cg-Tg(Plp1-cre/ ERT)3Pop/J, stock number 005975; strain name B6.Cg-Gt(ROSA)26Sor$^{tm14(CAG-tdTomato)Hze}$/J, stock number 007914; strain name NOD.CB17-*Prftdc^{scid}*/J, stock number 001303). PLP-mTomato mice were generated by breeding *PLP::CreER^{T2}* with *Rosa26^{tdTomato}* mice. The mice and genotyped as recommended by the manufacturer (Jackson Laboratory). Tamoxifen (Sigma) was dissolved in autoclaved corn oil (Sigma) at 20 mg/ml and mice were injected intraperitoneally 200 mg/kg daily for five consecutive days. The mice underwent an additional week of latency after tamoxifen administration to ensure that optimal Cre recombination was achieved. For this study adult male mice ranging from the age of 8–12 weeks were randomly allocated to experimental groups and sample size for any given experiment is detailed in the Figure legend.

This study was performed in accordance with Stanford University Animal Care and Use Committee guidelines. Daily care for the mice was provided by the Stanford Veterinary Service Center. Animals were housed in a controlled environment with 12-hour day/night cycle with optimal temperature and fed rodent chow *ad Iibitum.*

METHOD DETAILS

Inferior Alveolar Denervation Mouse Model—Mice were anesthetized with 2% isoflurane gas anesthesia and prepared sterilely for surgery. For IAN denervation, a curvilinear incision was made extending from the angle of the right mandible to the posterior neck. While protecting vascular structures, the posterior hemimandible was retracted laterally from the skull base to expose the IAN, which was transected prior to its entrance into the mandibular canal. Sham surgeries included all dissection and retraction but left the IAN intact. A minimum of two weeks postoperatively were allowed for complete nerve degeneration after denervation prior to commencing with subsequent experiments. For mandibular osteotomy surgery, an incision was made over the right masseter and skin was retracted from the operative zone. The masseter was divided sharply in the line of its fibers to expose the underlying buccal surface of the mandible. For full-thickness circular osteotomy, a 0.8 mm osteotomy was created using a micromotor drill. The periosteum was divided during osteotomy creation in both models. The masseter was then closed over the bone along with the skin using interrupted mattress sutures. Cellular transplantation was

performed by suspending FACS-isolated *PLP*-mTomato-positive Schwann cells in Matrigel matrix (ThermoFisher), which was then pipetted onto the mandible after osteotomy at a dose of 1 million cells in 5 μl of Matrigel. For *in vivo* administration of PDGF-AA, PTH, and OSM to the osteotomy site, growth factors were separately suspended in Matrigel at a concentration of 50 ng/μL. On POD 1 and 9, a Hamilton syringe was used to inject 8 mL of each growth factor suspension along the buccal surface of the mandible.

Mouse Skeletal Stem Cell (mSSC) and Schwann Culture—FACS-isolated mSSC were plated in tissue culture dishes coated with 0.1% gelatin and cultured in MEM alpha medium with 10% fetal bovine growth serum (FBS), 1% penicillin-streptomycin (P/S) under low hypoxia oxygen conditions (2% atmospheric oxygen, 7.5% CO_2). FACS-isolated *PLP*-mTomato-positive Schwann cells were plated on laminin-coated tissue culture dishes and cultured in DMEM F12 medium with 20% N2 supplement, 10% FBS, 1% P/S, and 10mM forskolin. Schwann cells were passaged until they reached 80% confluency and cells in this study were used from passage 1 or 2. mSSC and Schwann cells were isolated from male mice. For co-culture experiments, mSSC were plated on 24-well tissue culture plates coated with 0.1% gelatin and cultured in MEM alpha medium with 10% fetal bovine growth serum (FBS), 1% penicillin-streptomycin (P/S). *PLP*-mTomato-positive Schwann cells were seeded on 24-well hanging inserts with 0.4 mm pores (EMD Millipore) and placed into the 24-well plates seeded with mSSC, which did not allow cellular contact. Schwann cells were cultured in DMEM F12 medium with 20% N2 supplement, 10% FBS, 1% P/S, and 10mM forskolin. Control groups received Schwann cell media and no cells placed into the insert.

Histology Preparation—Dissected tissue samples were fixed in 2% paraformaldehyde (PFA) at 4°C overnight and washed with phosphate-buffered saline (PBS) the following day. The specimens were decalcified in 19% EDTA in PBS at 4°C for four weeks with a change of EDTA every 48 hours. Specimens were dehydrated and embedded in paraffin or optimal cutting temperature (OCT) and sectioned at 8μm. Representative sections were stained with Movat's modified pentachrome solution, hematoxylin and eosin, Alcian blue and nuclear fast red, or immunohistochemistry depending on the individual experiment.

Immunostaining—Histology slides were treated with PBS wash and permeabilization with 0.5% Triton X-100 (Sigma). Specimens were then incubated in blocking reagent and probed for primary antibody at 4°C overnight. The following day the specimens were washed with PBS, probed with a secondary Alexa-dye conjugated antibody, washed in PBS, and stained with DAPI to mark the nuclei. Lastly, the specimens were coverslipped and imaged. For immunocytochemistry, *PLP*-mTomato-positive cells were grown to confluency on glass coverslips, then fixed in 2% PFA at room temperature for 15 minutes. After washing with PBS, cells were permeabilized with 0.5% Triton X-100. Cells were incubated in blocking reagent then probed for primary antibody at 4°C overnight. The following day the specimens were washed with PBS, probed with a secondary Alexa-dye conjugated antibody, washed in PBS, and stained with DAPI to mark the nuclei. Coverslips were then mounted onto slides with Fluoromount-G (SouthernBiotech) and imaged.

µ-Computed Tomography Scanning—After harvesting, mandibles were fixed in 2% PFA at 4°C overnight and then washed and left in PBS. Scans were completed with Bruker SkyScan 1276 at 10 µm resolution. Reconstruction was performed with NRecon software (Bruker), and 3D solid volume images were produced CTVol (Bruker). Bone volume per tissue volume was measured using a standardized region of interest of 0.8mm (osteotomy size) in CTAn (Bruker).

EdU Analysis *in vivo*—To assess *in vivo* proliferation activity in our study we used Click-iT™ EdU Alexa Fluor™ 488 Imaging Kit (ThermoFisher). Briefly, mice were injected intraperitoneally with 15 mg EdU/kg at POD 0 and POD 9. Mandibles were harvested at POD 10 and received OCT histological preparation as listed above. Specimens were fixed, permeabilized, and treated with the Click-it reaction. The slides were coverslipped and imaged on Lecia DMI6000B inverted microscope.

Isolectin Staining in *vivo*—Mice underwent denervation or sham surgery. Two weeks after these procedures, mice were anesthetized with 2% isoflurane and administered fluorophore-tagged isolectin GS-IB4 (isolectin) via retro-orbital injection to reach the intravascular space. The compound was allowed to circulate for 15 minutes, at which point intracardiac aspiration of blood was performed to allow optimal isolectin staining. The mice were euthanized and mandibles were harvested. Specimens were fixed, decalcified and sectioned as previously described.

Fluorescent Activated Cell Sorting—The detailed steps listed in Gulati et al., 2018 were followed to isolate mSSC. Briefly, bones were dissected and serially digested in collagenase digestion buffer at 37°C for three 30-minute intervals under constant agitation. The dissociated cells were filtered through a 70 µm mesh filter, pelted at 1350 rpm at 4°C and stained for CD45, Ter119, CD202b, Thy 1.1, Thy 1.2, CD105, CD51, 6C3, and a streptavidin-conjugated CD200. Cells were stained with propidium iodide (PI) to exclude dead cells. Fluorescent activated cell sorting (FACS) was performed on FACS Aria II Instrument (BD Biosciences, San Jose, CA) using a 70 µm nozzle. To isolate Schwann cells, a similar technique was used as described above. Since the *PLP::CreER^{T2};R26^{mTomato}* (PLP Tomato) mouse harbors an endogenous tomato (red) fluorochrome, staining with antibodies was not required. DAPI was used as a viability stain and live *PLP*-positive Schwann cells were sorted based upon mTomato expression.

Colony Forming Unit Assay—Colony forming unit assays were determined as detailed in Chan et al. (2015). Briefly, skeletal stem cells were cultured for two weeks in conditions described above. After two weeks, the cells were examined under phase microscopy using a cloning ring for quantification. Five biological replicates were used for each experiment, and each experiment was performed three times. After counting colonies as described above, mean colony counts were calculated and compared across groups using unpaired t tests.

Osteogenic Differentiation Assay—FACS-isolated mSSC harvested from uninjured and POD10 mandibles were cultured in 96-well plates over a course of two weeks at low-oxygen conditions, then incubated with osteogenic medium for an additional two weeks with media changes every 48 hours. The cells were then washed with PBS and ultra-pure water

and fixed with 100% ethanol. Cells were then stained with alizarin red solution at room temperature. Cells were washed with ultra-pure water and imaged immediately. After imaging, the cells were incubated with methanol/acetic acid mixture and alizarin red protein concentration was detected at 450 nm using NanoDrop™ 0ne^c Microvolume UV-Vis Spectrophotometer (ThermoFisher). Values from uninjured, innervated P0D10 and denervated P0D10 mandible defects were compared using ANOVA.

RNA Isolation and Real Time qPCR—Total RNA was isolated from mSSC FACS-sorted into TRIzol (Invitrogen) following the manufacturer's protocol (Invitrogen). RNA was reverse transcribed using SuperScript VILO (ThermoFisher) following standard protocol. cDNA was then amplified using TaqMan PreAmp Master Mix (ThermoFisher) and then used in qPCR with PowerUp SYBR Green (Applied Biosystems) following standard protocol. For controls, GAPDH was used as positive control gene and water as no template control (negative control). ABI-7900 Real Time PCR instrument was used to generate cycle threshold (CT) values.

Imaging and Analysis—Confocal microscopy imaging was performed with a Leica TCS SP8 X confocal microscope (Leica Microsystems) with objective lens (20x and 40x HC PL APO IMM CORR CS2 $H_2$0/Glycerol/oil, N.A. 0.75) located in the Cell Sciences Imaging Facility (Stanford University, Stanford, CA). Raw image stacks were into imported Fiji (National Institutes of Health) for analysis. Fiji software was then used to generate two-dimensional confocal micrographs and to quantify intensity of fluorophore expression. Images in our study are represented as average maximal projection of our 8 mm sections with their brightness and contrast were adjusted accordingly for each designated color channels (blue, red, and green).

QUANTIFICATION AND STATISTICAL ANALYSIS

Fluorophore Intensity Quantification—Raw images from stereoscopic microscopy fluorescent imaging of PLP Tomato mice were imaged and loaded into ImageJ. Intensity of the region of interest (IAN) and background area was recorded multiples times per biological replicate (Figures 1A and 1C). Region of interest intensity was corrected to the background intensity. For quantification of *PLP* and *PGP9.5* expression in immune-stained tissue sections, green or red intensity of the nerve was measured and corrected to the background intensity in ImageJ (Figures 1D and 1E). Similarly, tissue sections from 6-month denervation lineage trace of PLP Tomato mouse were imaged with confocal microscopy and ImageJ was used to quantify corrected mean intensity of red fluorescence of the nerve (Figures 1F and 1G). Mean corrected intensity is presented and was compared using unpaired t tests.

Alcian Blue Intensity Quantification—Raw images from light microscopy imaging of Alcian blue stained mandibular tissue sections were loaded into ImageJ. Color thresholding was used to identify blue staining. Intensity was measured and corrected to background intensity (Figure 2E). The average blue intensity of innervated and denervated mandible defects were compared with unpaired t tests to compare cartilage levels between conditions.

μ-Computed Tomography Scanning Quantification—A standard region of interest of 0.8 mm was applied to the bone defect area in μCT reconstructions from 5 biological replicates per condition using CTAn software (Bruker) to determine percent bone volume per tissue volume. Identification of bone tissue is based upon tissue density via an automatic thresholding process in CTAn. Nearby normal mandible bone and attached muscle were used as a positive control (bone) and negative control (muscle) to confirm appropriate density thresholding and bone identification (Figures 2C, 2D, 4E, and 4H). Mean values of bone volume per tissue volume were compared across POD 10, 20 and 30 using unpaired t tests.

EdU Quantification—Five biological replicates per condition (uninjured, innervated POD 10, denervated POD 10) were imaged with fluorescence light microscopy and quantified with ImageJ by counting the number of EdU positive (green) cells in the bone defect area (Figures 2F and 2G). Mean counts were compared with ANOVA.

FACS Quantification—Gating was performed in FlowJo (FlowJo) to determine cell counts from individual sorts. Five biological replicates were used per condition in each experiment, with 3 technical replicates per experiment. Mean cell frequencies were normalized to cell frequencies from uninjured mandibles to express fold change from uninjured state (Figures 3B–3D and 3F). Mean percentage of cell population per parent cell population was determined (Figures 3E and 3G). Values were compared across conditions with unpaired t tests for each POD.

Real Time qPCR Analysis—To quantify relative gene expression, the $2^{(-\Delta\Delta CT)}$ method was used. Briefly, change in threshold cycle (ΔCT) was obtained by calculating the difference between threshold cycle (CT) of the target genes (PDGF-AA, PTH, OSM, PDGFRα, PTH1R, and OSMR) and the housekeeping gene (GAPDH). $\Delta\Delta$CT was calculated by taking the difference between ΔCT of our treatment group targets (POD 10 mSSC or *PLP*-mTomato-positive Schwann cells) and ΔCT of our reference group (mSSC GAPDH or *PLP*-mTomato-positive Schwann cell GAPDH). The $\Delta\Delta$CT was raised to the power of negative 2 to obtain relative gene expression values. Normalized gene expression values are presented as fold change relative to the reference sample (Figures S4A and S4B). Oligonucleotide sequences are listed in Table S1.

Statistics—For all experiments, n is equal to the number of animals used unless otherwise specified. The number of biological and technical replicates are specified in Figure legends. All graphs plot the individual values with error bars to represent standard error of the mean. Unpaired t tests and ANOVA were used to compare values for all experiments except where indicated. Prism software (Graphpad) was used for all analyses and a *p* value of 0.05 or less was set as a threshold for statistical significance. For all figures, asterisks denote statistical significance at the following levels: $*p < 0.05$, $**p < 0.01$, $***p < 0.001$, $****p < 0.0001$.

Supplementary Material

Refer to Web version on PubMed Central for supplementary material.

ACKNOWLEDGMENTS

REFERENCES

Ali MN, Kobayashi T, Tanaka M, Ohshima H, Ejiri S, and Saito C. (2012). Effects of intermittent parathyroid hormone treatment on new bone formation during distraction osteogenesis in the rat mandible. Oral Surg. Oral Med. Oral Pathol. Oral Radiol 114, e36–e42.

Aro H. (1985). Effect of nerve injury on fracture healing. Callus formation studied in the rat. Acta Orthop. Scand 56, 233–237. [PubMed: 4036573]

Brockes JP (1984). Mitogenic growth factors and nerve dependence of limb regeneration. Science 225, 1280–1287. [PubMed: 6474177]

Carr MJ, Toma JS, Johnston APW, Steadman PE, Yuzwa SA, Mahmud N, Frankland PW, Kaplan DR, and Miller FD (2019). Mesenchymal precursor cells in adult nerves contribute to mammalian tissue repair and regeneration. Cell Stem Cell 24, 240–256.e9. [PubMed: 30503141]

Chan CK, Seo EY, Chen JY, Lo D, McArdle A, Sinha R, Tevlin R, Seita J, Vincent-Tompkins J, Wearda T, et al. (2015). Identification and specification of the mouse skeletal stem cell. Cell 160, 285–298. [PubMed: 25594184]

Chan CKF, Gulati GS, Sinha R, Tompkins JV, Lopez M, Carter AC, Ransom RC, Reinisch A, Wearda T, Murphy M, et al. (2018). Identification of the human skeletal stem cell. Cell 175, 43–56.e21. [PubMed: 30241615]

Chiego DJ Jr., Klein RM, and Avery JK (1981). Tritiated thymidine autoradiographic study of the effects of inferior alveolar nerve resection on the proliferative compartments of the mouse incisor formative tissues. Arch. Oral Biol 26, 83–89. [PubMed: 6944031]

Clements MP, Byrne E, Camarillo Guerrero LF, Cattin AL, Zakka L, Ashraf A, Burden JJ, Khadayate S, Lloyd AC, Marguerat S, et al. (2017). The wound microenvironment reprograms Schwann cells to invasive mesenchymal-like cells to drive peripheral nerve regeneration. Neuron 96, 98–114.e7. [PubMed: 28957681]

Costa MA, Barbosa A, Neto E, Sá-e-Sousa A, Freitas R, Neves JM, Magalhães-Cardoso T, Ferreirinha F, and Correia-de-Sá P. (2011). On the role of subtype selective adenosine receptor agonists during proliferation and osteogenic differentiation of human primary bone marrow stromal cells. J. Cell. Physiol 226, 1353–1366. [PubMed: 20945394]

Dysart PS, Harkness EM, and Herbison GP (1989). Growth of the humer-us after denervation. An experimental study in the rat. J. Anat 167, 147–159. [PubMed: 2630528]

Espinosa-Medina I, Outin E, Picard CA, Chettouh Z, Dymecki S, Consalez GG, Coppola E, and Brunet JF (2014). Neurodevelopment. Parasympathetic ganglia derive from Schwann cell precursors. Science 345, 87–90. [PubMed: 24925912]

Gharibi B, Abraham AA, Ham J, and Evans BA (2011). Adenosine receptor subtype expression and activation influence the differentiation of mesenchymal stem cells to osteoblasts and adipocytes. J. Bone Miner. Res 26, 2112–2124. [PubMed: 21590734]

Gulati GS, Murphy MP, Marecic O, Lopez M, Brewer RE, Koepke LS, Manjunath A, Ransom RC, Salhotra A, Weissman IL, et al. (2018). Isolation and functional assessment of mouse skeletal stem cell lineage. Nat. Protoc 13, 1294–1309. [PubMed: 29748647]

Hsieh TY, Funamura JL, Dedhia R, Durbin-Johnson B, Dunbar C, and Tollefson TT (2019). Risk factors associated with complications after treatment of mandible fractures. JAMA Facial Plast. Surg 21, 213–220. [PubMed: 30676610]

Jilka RL, Weinstein RS, Bellido T, Roberson P, Parfitt AM, and Mano-lagas SC (1999). Increased bone formation by prevention of osteoblast apoptosis with parathyroid hormone. J. Clin. Invest 104, 439–446. [PubMed: 10449436]

Johnston AP, Yuzwa SA, Carr MJ, Mahmud N, Storer MA, Krause MP, Jones K, Paul S, Kaplan DR, and Miller FD (2016). Dedifferentiated Schwann cell precursors secreting paracrine factors are required for regeneration of the mammalian digit tip. Cell Stem Cell 19, 433–448. [PubMed: 27376984]

Kaukua N, Shahidi MK, Konstantinidou C, Dyachuk V, Kaucka M, Fur-lan A, An Z, Wang L, Hultman I, Ahrlund-Richter L, et al. (2014). Glial origin of mesenchymal stem cells in a tooth model system. Nature 513, 551–554. [PubMed: 25079316]

Li Z, Hao J, Duan X, Wu N, Zhou Z, Yang F, Li J, Zhao Z, and Huang S. (2017). The role of semaphorin 3A in bone remodeling. Front. Cell. Neurosci 11, 40. [PubMed: 28293171]

Ma Y, Nyman JS, Tao H, Moss HH, Yang X, and Elefteriou F. (2011). β2-Adrenergic receptor signaling in osteoblasts contributes to the catabolic effect of glucocorticoids on bone. Endocrinology 152, 1412–1422. [PubMed: 21266510]

Macica CM, Liang G, Lankford KL, and Broadus AE (2006). Induction of parathyroid hormone-related peptide following peripheral nerve injury: role as a modulator of Schwann cell phenotype. Glia 53, 637–648. [PubMed: 16470617]

Marecic O, Tevlin R, McArdle A, Seo EY, Wearda T, Duldulao C, Walmsley GG, Nguyen A, Weissman IL, Chan CK, and Longaker MT (2015). Identification and characterization of an injury-induced skeletal progenitor. Proc. Natl. Acad. Sci. USA 112, 9920–9925. [PubMed: 26216955]

Minoux M, Holwerda S, Vitobello A, Kitazawa T, Kohler H, Stadler MB, and Rijli FM (2017). Gene bivalency at Polycomb domains regulates cranial neural crest positional identity. Science 355, eaal2913. [PubMed: 28360266]

Negishi-Koga T, Shinohara M, Komatsu N, Bito H, Kodama T, Friedel RH, and Takayanagi H. (2011). Suppression of bone formation by osteoclastic expression of semaphorin 4D. Nat. Med 17, 1473–1480. [PubMed: 22019888]

Parfejevs V, Debbache J, Shakhova O, Schaefer SM, Glausch M, Wegner M, Suter U, Riekstina U, Werner S, and Sommer L. (2018). Injury-activated glial cells promote wound healing of the adult skin in mice. Nat. Commun 9, 236. [PubMed: 29339718]

Ransom RC, Carter AC, Salhotra A, Leavitt T, Marecic O, Murphy MP, Lopez ML, Wei Y, Marshall CD, Shen EZ, et al. (2018). Mechanoresponsive stem cells acquire neural crest fate in jaw regeneration. Nature 563, 514–521. [PubMed: 30356216]

Recidoro AM, Roof AC, Schmitt M, Worton LE, Petrie T, Strand N, Ausk BJ, Srinivasan S, Moon RT, Gardiner EM, et al. (2014). Botulinum toxin induces muscle paralysis and inhibits bone regeneration in zebrafish. J. Bone Miner. Res 29, 2346–2356. [PubMed: 24806738]

Richardson PM, McGuinness UM, and Aguayo AJ (1980). Axons from CNS neurons regenerate into PNS grafts. Nature 284, 264–265. [PubMed: 7360259]

Rinkevich Y, Lindau P, Ueno H, Longaker MT, and Weissman IL (2011). Germ-layer and lineage-restricted stem/progenitors regenerate the mouse digit tip. Nature 476, 409–413. [PubMed: 21866153]

Rinkevich Y, Montoro DT, Muhonen E, Walmsley GG, Lo D, Hasegawa M, Januszyk M, Connolly AJ, Weissman IL, and Longaker MT (2014). Clonal analysis reveals nerve-dependent and independent roles on mammalian hind limb tissue maintenance and regeneration. Proc. Natl. Acad. Sci. U SA 111, 9846–9851.

Silva WN, Leonel C, Prazeres PHDM, Sena IFG, Guerra DAP, Heller D, Diniz IMA, Fortuna V, Mintz A, and Birbrair A. (2018). Role of Schwann cells in cutaneous wound healing. Wound Repair Regen. 26, 392–397. [PubMed: 30098299]

Tay AB, Lai JB, Lye KW, Wong WY, Nadkarni NV, Li W, and Bautista D. (2015). Inferior alveolar nerve injury in trauma-induced mandible fractures. J. Oral Maxillofac. Surg 73, 1328–1340. [PubMed: 25914133]

Uesaka T, Nagashimada M, and Enomoto H. (2015). Neuronal differentiation in Schwann cell lineage underlies postnatal neurogenesis in the enteric nervous system. J. Neurosci 35, 9879–9888. [PubMed: 26156989]

Weinberg HJ, and Spencer PS (1978). The fate of Schwann cells isolated from axonal contact. J. Neurocytol 7, 555–569. [PubMed: 722316]

Zhao H, Feng J, Seidel K, Shi S, Klein O, Sharpe P, and Chai Y. (2014). Secretion of shh by a neurovascular bundle niche supports mesenchymal stem cell homeostasis in the adult mouse incisor. Cell Stem Cell 14, 160–173 [PubMed: 24506883]

Highlights

- Denervation of the mandible impedes bone healing by impairing skeletal stem cells

- Bone healing requires Schwann cell paracrine factors for proper stem cell function

- Schwann cells and their signaling products rescue denervated mandibular healing
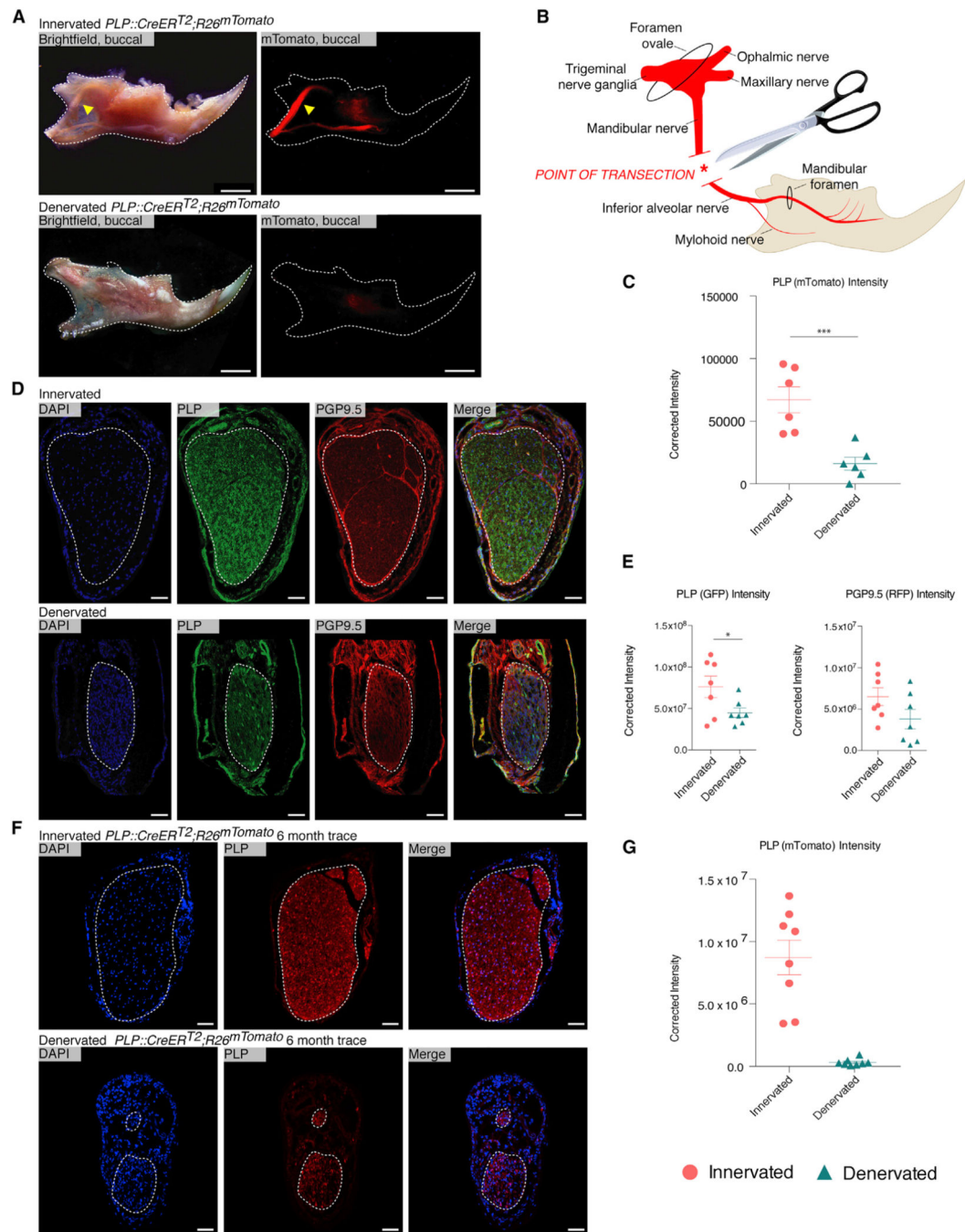
Figure 1. Proximal Mandibular Denervation by Complete IAN Disruption Induces Nerve Degeneration and Schwann Cell Depletion

(A) Whole-mount microscopy of PLP Tomato mandibles 2 weeks after sham operation (top) and mandibular denervation (bottom). Yellow arrows denote the IAN (top). n = 3.

(B) Schematic illustrating mouse mandibular anatomy and denervation strategy.

(C) Red fluorescence quantification of whole-mount PLP Tomato innervated (circles) and denervated (triangles) mandibles. n = 3.

(D) Staining of innervated (top) and denervated (bottom) mandibles imaged with confocal microscopy 2 weeks after denervation. PLP marks Schwann cells (green), and PGP 9.5 marks axons (red).

(E) Quantification (left) of PLP expression (green) in innervated (circles) and denervated (triangles) from (D). Quantification (right) of PGP9.5 expression (red) in innervated (circles) and denervated (triangles) from (D). n = 5.

(F) Contralateral (upper) and denervated (lower) mandibular canals of a PLP Tomato mouse imaged with confocal microscopy 6 months after denervation. n = 1.

(G) Quantification of PLP expression (red) in denervated (triangles) and contralateral (circles) mandibles from (F).

Scale bars, 1 mm (A) and 50 μm (D and F). Images are counterstained with DAPI (blue), with white dotted line outlining the mandible (A) or the IAN (D and F). Error bars denote SEM (C, E, and G), and statistical comparisons were made using t tests (C and E). No statistical comparison was made for the 6-month denervation trace (one biological replicate).
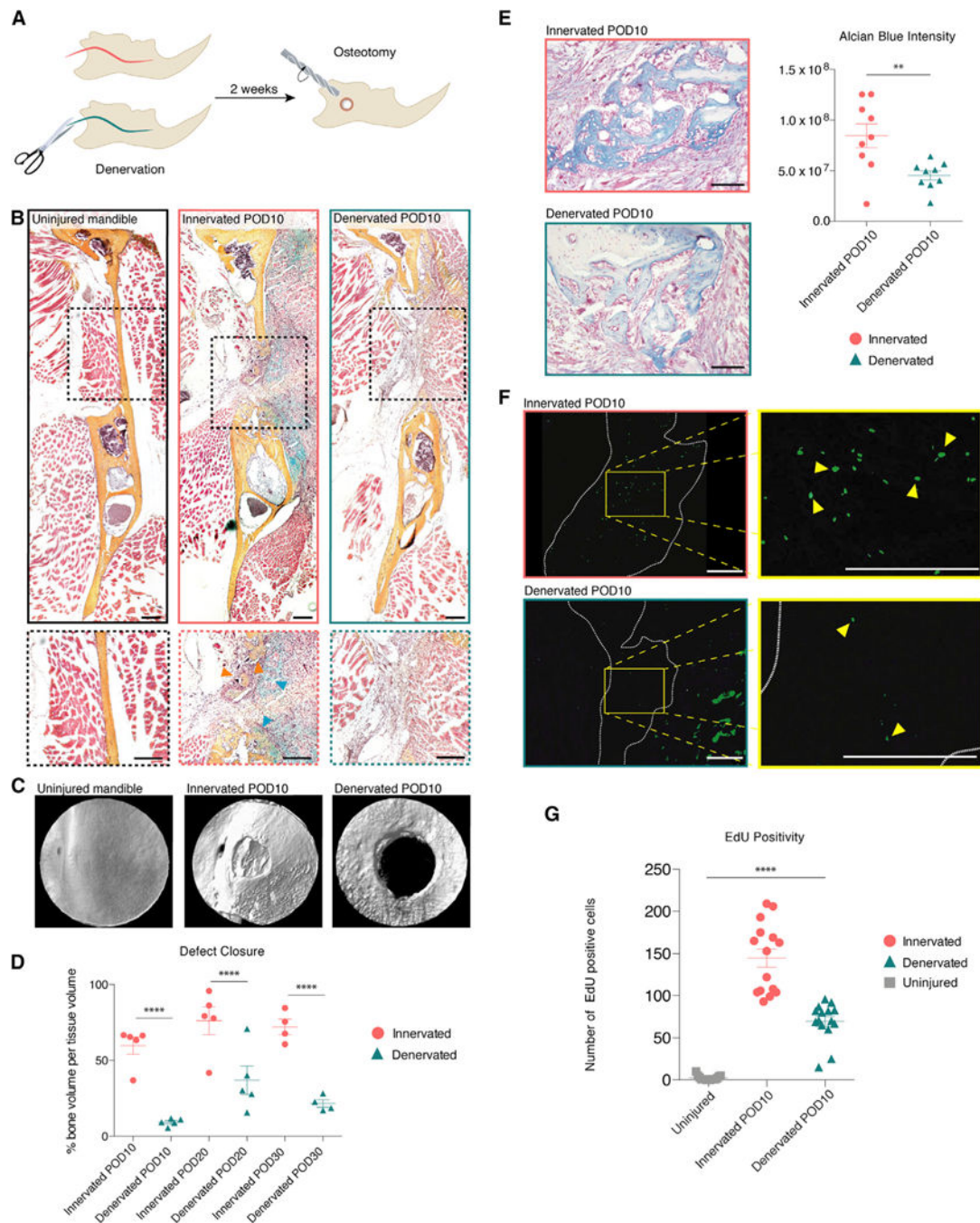
Figure 2. Mandibular Healing Exhibits Nerve Dependency with Impaired Progenitor Activity in Denervated Mandibles

(A) Schematic of experimental design.

(B) Pentachrome stain of uninjured mandible (left), innervated defect (middle), and denervated defect (right) harvested at POD 10. Bottom panels zoom in on the defect area. Orange arrows denote new bone mineralization and blue arrows denote cartilage formation (middle bottom). n = 10.

(C) Three-dimensional (3D) reconstruction of μCT scan of uninjured (left), innervated (middle), and denervated (right) mandible defects.

(D) Quantification comparing bone volume per tissue volume at PODs 10, 20, and 30 after mandibular osteotomy in innervated (circles) and denervated (triangles) mandibles. n = 5

(E) Alcian blue staining identifies cartilageat POD 10after osteotomy in innervated (top left) and denervated (bottom left) mandible defects. Quantification (right) of blue staining. n = 5.

(F) EdU labeling (green) at POD 10 (innervated, upper panel, and denervated, bottom panel). Yellow outline signifies zoomed area (right). White dotted line indicates mandibular defect area. Yellow arrows mark EdU positive cells (right).

(G) Quantification comparing EdU positivity in uninjured (squares), innervated defect (circles), and denervated defect (triangles). n = 5.

Scale bars, 200 μm (B and F) and 100 mm (E). μCT resolution, 10 μm (C). Error bars denote SEM (D and G). Statistical comparisons were made using t tests (D) and ANOVA (G). See also Figure S1.
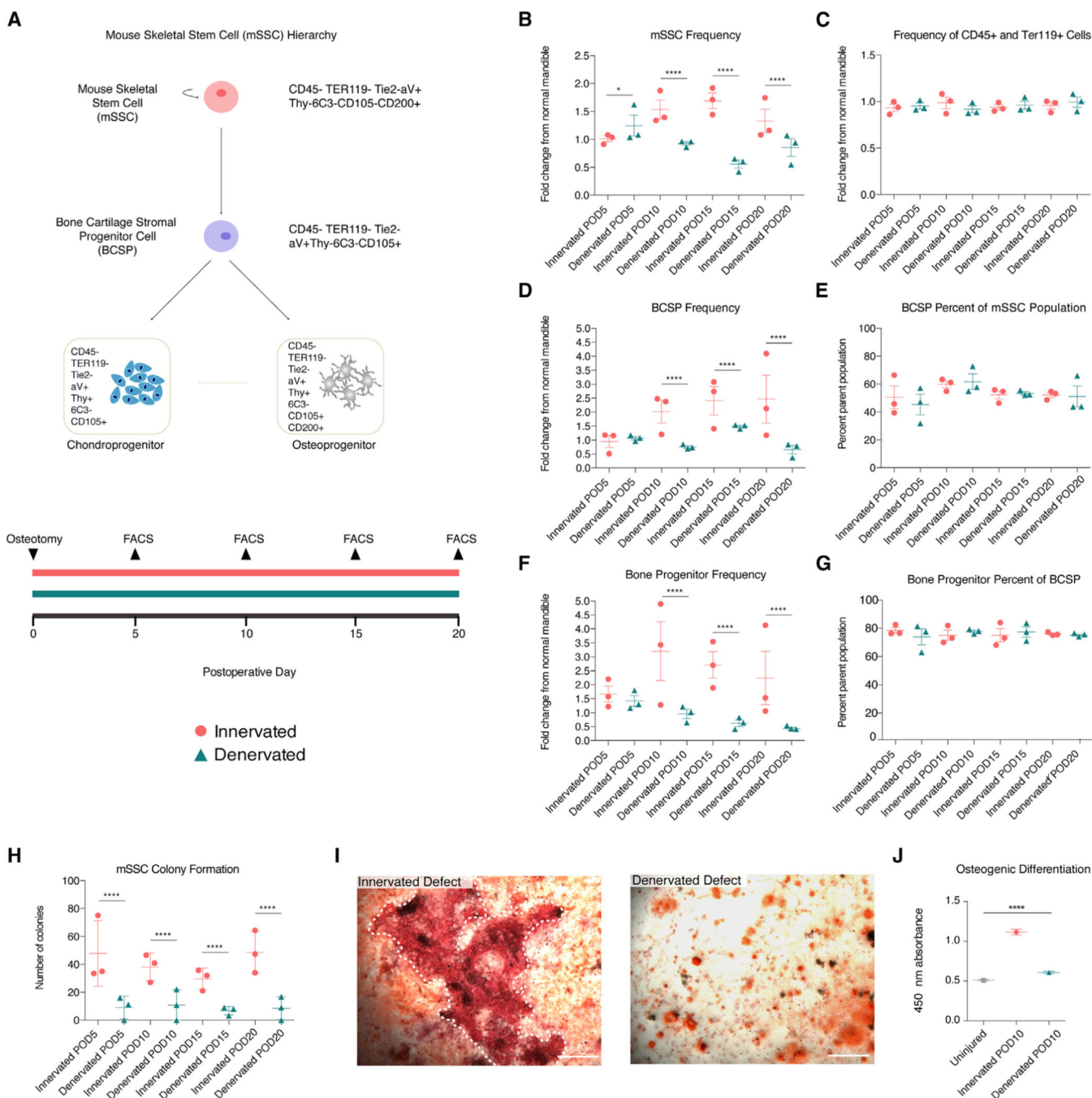
Figure 3. Mouse Skeletal Stem Cells in Healing Mandible Bone Are Nerve Dependent

(A) Schematic of the mSSC hierarchy (top) and experimental timeline (bottom).

(B) mSSC cellular frequencies post-osteotomy in innervated (circles) and denervated (turquoise) mandibles at multiple postoperative days.

(C) Cellular frequencies of CD45-positive and Terr119-positive cells in innervated (circles) and denervated (triangles) mandibles.

(D) BCSP cellular frequencies post-osteotomy in innervated (circles) and denervated (triangles) mandibles.

(E) Percentage BCSP cells within parent mSSC population post-osteotomy in innervated (circles) and denervated (triangles) mandibles.

(F) Bone progenitor cellular frequencies post-osteotomy in innervated (circles) and denervated (triangles) mandibles.

(G) Percentage bone progenitors within parent BCSP population post-osteotomy in innervated (circles) and denervated (turquoise triangles) mandibles.

(H) Colony formation units of mSSC isolated from innervated (circles) and denervated (triangles) mandibles.

(I) Alizarin red staining of POD 10 mSSCs from innervated (left) and denervated (right) defects. White dotted line indicates large bony nodule (left).

(J) Quantification of alizarin red absorbance after osteogenic differentiation.

Scale bars, 400 μm (I). For (B)–(H), n = 5 biological replicates per condition with three technical replicates. Cellular frequencies were normalized to cellular frequencies from uninjured mandibles. For (I) and (J), n = 10 biological replicates per condition with three technical replicates. Error bars represent SEM (B–H and J), and statistical comparisons were made using t tests (B–H) and ANOVA (J). See also Figure S1
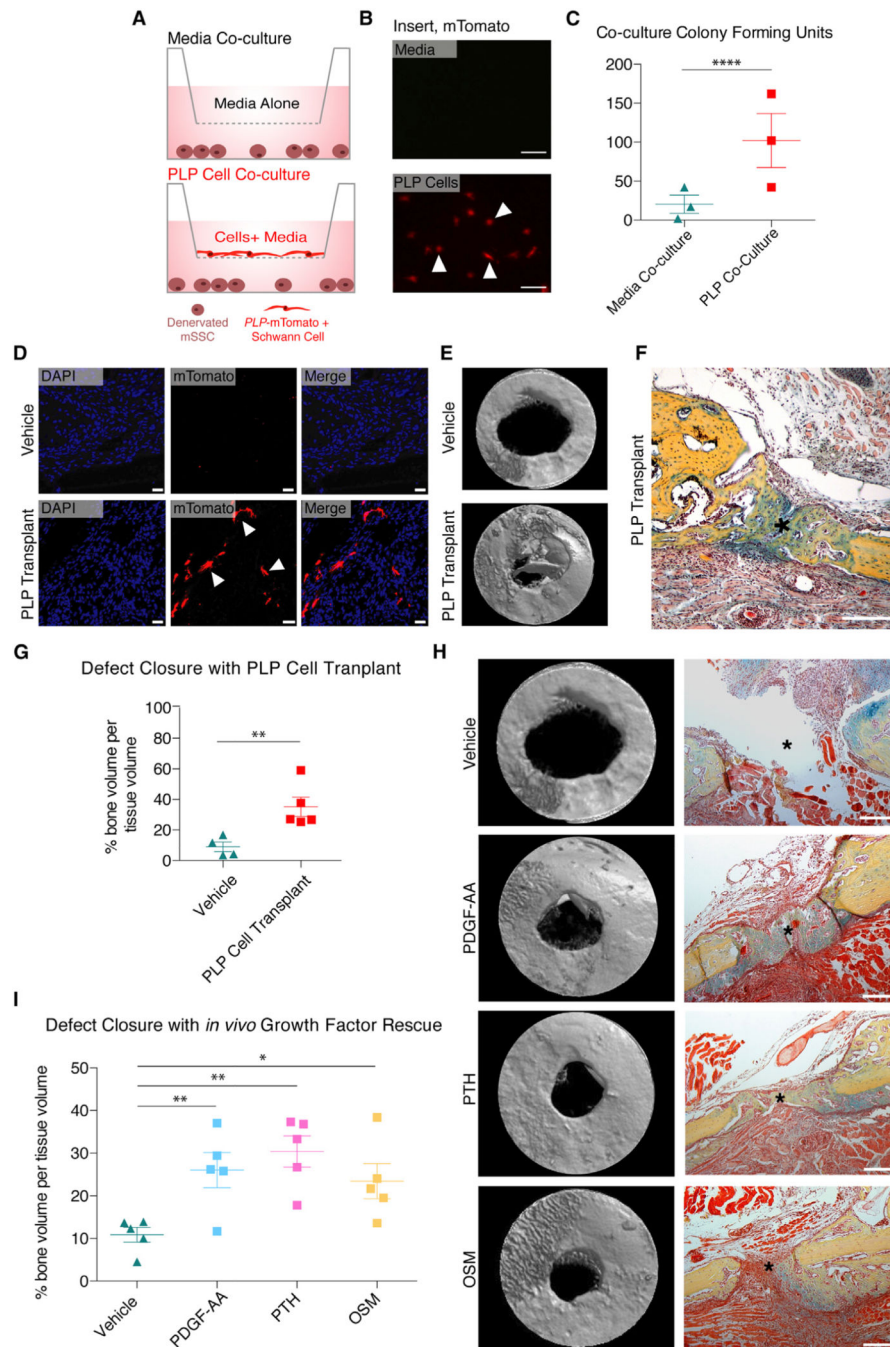
Figure 4. Schwann Cells and Their Secreted Factors Rescue Denervated Healing

(A) Illustration of mSSC co-culture experiments.

(B) Fluorescent imaging of insert seeded with Schwann cell media (top panel) and insert seeded with *PLP*-mTomato-positive Schwann cells (bottom panel) after 2 weeks in culture. Arrows mark example *PLP*-mTomato-positive Schwann cells (bottom).

(C) Colony formation units of mSSC from co-culture with media alone (triangles) versus Schwann cells (squares) n = 5.

(D) Confocal microscopy showing no engraftment (top panel) versus engraftment (bottom panel) of *PLP*-mTomato-positive Schwann cells in denervated mandibles after treatment with Matrigel (vehicle, top panel) or Schwann cells (PLP transplant, bottom panel). Arrows mark example *PLP*-mTomato-positive Schwann cells. n = 4.

(E) Three-dimensional reconstruction of μCT scans of denervated mandible defects at POD 10 after treatment with vehicle (top panel) versus *PLP*-mTomato-positive Schwann cell transplantation (bottom panel). n = 4.

(F) Pentachrome staining of denervated mandible defect treated with *PLP*-mTomato-positive Schwann cell transplantation at time of osteotomy. n = 5.

(G) Quantification comparing bone volume per tissue volume in denervated mandibular defects treated with vehicle (triangles) versus Schwann cell transplant (squares). n = 4.

(H) Three-dimensional reconstruction of μCT scans and corresponding pentachrome stains of denervated mandibular defects treated with PDFG-AA, PTH, OSM, and Matrigel vehicle at PODs 1 and 5 after osteotomy. n = 5.

(I) Quantification comparing bone volume per tissue volume in denervated mandibular defects treated with vehicle (triangles) versus PDFG-AA (blue squares), PTH (pink squares), and OSM (yellow squares). n = 5.

Scale bars, 200 μm (F and H). μCT resolution, 10 μm (E and H). Asterisk denotes center of circular osteotomy (F and H). Error bars represent SEM, and statistical comparisons were made using t tests (C, G, and I). See also Figures S2–S4. Please note the experiments in (E) (PLP-Transplant) and (H) (Growth Factor Transplant) were performed at the same time and therefore they have the same Vehicle control group (Matrigel alone), which appears twice in this figure to serve as a reference to the experimental groups

KEY RESOURCES TABLE

REAGENT or RESOURCE Antibodies	SOURCE	IDENTIFIER
Rat anti-mouse CD90.1 (Thy1.1) clone: HIS51, APC-eFluor780	ThermoFisher	Cat#47-0900-82
Rat anti-mouse CD90.2 (Thy1.2) clone: 53-2.1, APC-eFluor780	ThermoFisher	Cat#47-0902-82
Rat anti-mouse CD105, clone: MJ7/18, biotin	ThermoFisher	Cat#13-1051-85
Rat anti-mouse CD200, clone: OX-90, BV605	BD Biosciences	Cat#745255
Rat anti-mouse CD45, clone: 30-F11, PE-Cy5	Biolegend	Cat#103110
Rat anti-mouse TER119, clone: TER119, PE-Cy5	ThermoFisher	Cat#15-5921-81; RRID: AB_468809
Rat anti-mouse TIE2 (CD202B), clone: TEK4	ThermoFisher	Cat#14-5987-81; RRID: AB_466847
Rat anti-mouse ITGAV CD51, clone: RMV-7, PE	BD Biosciences	Cat#551187; RRID: AB_394088
Goat anti-rat IgG secondary antibody, Qdot 605	ThermoFisher	Cat#Q-11601MP; RRID: AB_2556476
Alexa Fluor 680 Fluorophore Antibody Labeling Kit	ThermoFisher	Cat#A20188
Mouse anti-mouse anti-PGP9.5, clone: 13C4	Abcam	Cat#Ab8189; RRID: AB_306343
Rabbit anti-mouse myelin PLP	Abcam	Cat#Ab28486; RRID: AB_776593
Rabbit anti-mouse S100	Abcam	Cat#Ab868; RRID: AB_306716
Rabbit anti-mouse CD34	Abcam	Cat#Ab81289; RRID: AB_1640331
Rabbit anti-mouse Collagen 1	Abcam	Cat#Ab34710; RRID: AB_731684
Rabbit anti-mouse Runx2	Abcam	Cat#Ab23981; RRID: AB_777785
Goat anti-Rabbit IgG (H+L) Superclonal Secondary Antibody, Alexa Fluor 488	ThermoFisher	Cat#A28175; RRID: AB_2536161
Goat anti-Rabbit IgG (H+L) Highly Cross-Adsorbed Secondary Antibody, Alexa Fluor 647	ThermoFisher	Cat#A-21245; RRID: AB_2535813
Isolectin GS-IB4 From Griffonia simplicifolia, Alexa Fluor 647 Conjugate	ThermoFisher	Cat#I32450
Chemicals, Peptides, and Recombinant Proteins		
Tamoxifen	Sigma	Cat#T5648
Corn Oil	Sigma	Cat#C8267
Alizarin Red S	Sigma	Cat#H7904
Alcian Blue	Sigma	Cat#83157
Ammonium Hydroxide	Fisher Chemical	Cat#A669-500
Hematoxylin	Sigma	Cat#H3136
Brilliant Crocein	ChemCruz	CAS# 5413-75-2
Acid Fuchsin	Sigma	Cat#F8129

REAGENT or RESOURCE Antibodies	SOURCE	IDENTIFIER
Ferric Chloride	PolyScientific	CAS#10025-77-1
Acetic Acid	EMD Millipore	Cat#AX0073
Phosphotungstic Acid	Sigma	Cat#P4006
Saffron	Sigma	Cat#S8381
Nuclear Fast Red solution	Sigma	CAS# 6409-77-4
Eosin Y solution, alcoholic	Sigma	Cat#HT1101128
Ethanol	Gold Shield	Cat#64-17-5
Permount	Fisher Chemicals	Cat#SP15
Triton X-100	Sigma	Cat#X100
DAPI (4', 6-Diamido-2-Phenylindole, Dihydrochloride)	ThermoFisher	Cat#D1306
Millicell Cell Culture Inserts	EMD Millipore	Cat#MCHT24H48
Recombinant Murine PDGF-AA	PeproTech	Cat#315-17
Parathyroid Hormone (PTH) (1-34), Human	GenScript	Cas# 52232-67-4
Recombinant Human Oncostatin M (OSM) Protein	R&D Systems	Cat#295-OM/CF
Corning Matrigel Membrane Matrix	ThermoFisher	Cat#356234
Fluoromount-G	SouthernBiotech	Cat#0100-01
Critical Commercial Assays		
Click-iT EdU Alexa Fluor 488 Imaging Kit	ThermoFisher	Cat#C10337
StemPro Osteogenesis Differentiation Kit	ThermoFisher	Cat#A1007201
SuperScript VILO cDNA Synthesis Kit	ThermoFisher	Cat#11755-050
TaqMan PreAmp Master Mix	ThermoFisher	Cat#4391128
PowerUp SYBR Green	Applied Biosystems	Cat#A25741
Experimental Models: Organisms/Strains		
C57BL/6J	The Jackson Laboratory	Cat#000664
B6.Cg-Tg(Plp1-cre/ERT)3Pop/J	The Jackson Laboratory	Cat#005975
B6.Cg-Gt(ROSA)26Sor$^{tm14(CAG-tdTomato)Hze}$/J	The Jackson Laboratory	Cat#007914
NOD.CB17-Prkdcscid/J	The Jackson Laboratory	Cat# 001303
Oligonucleotides		

REAGENT or RESOURCE Antibodies	SOURCE	IDENTIFIER
See Table S1		
Software and Algorithms		
NRecon	Bruker	N/A
CTAn	Bruker	N/A
CTVol	Bruker	N/A
ImageJ	National Institutes of Health	RRID:SCR_002285
Adobe Photoshop CC	Adobe	RRID:SCR_014199
Adobe Illustrator CC	Adobe	RRID:SCR_010279
Prism 5	GraphPad	RRID:SCR_002798